Optimising control of stationary cross-flow vortices excited by surface roughness

Christian Thomas[1] and Shahid Mughal[2]
[1)]*School of Mathematical and Physical Sciences, Macquarie University, NSW 2109, Australia*
[2)]*Department of Mathematics, Imperial College London, London, SW7 2AZ, UK*

(*Electronic mail: christian.thomas@mq.edu.au)

(Dated: 29 September 2022)

Stationary cross-flow vortices are excited within the swept Hiemenz boundary layer via surface roughness and actively controlled using an optimally configured control device. Control is modelled using localised wall motion, but in practice the optimisation strategy could be applied to other laminar flow control technologies. A sensor-control iterative procedure, based on solutions of the forward and adjoint linearised Navier–Stokes equations, is applied to both feedforward and feedback loop systems. The former strategy only allows the control settings to be configured once, while the latter approach permits the repeated reoptimisation of the control device. Surface roughness establishes a stationary cross-flow disturbance with a pre-defined set of flow conditions, but an unknown amplitude and phase. A sensor measures the local amplitude of the perturbation and relays the information to the control mechanism. Solutions of the adjoint linearised Navier–Stokes equations are coupled with the sensor measurements to configure and optimise the control mechanism, and establish an anti-phase wave that brings about destructive wave interference. The amplitude of the stationary cross-flow instability is reduced by an order 10^3 for the feedforward system, while amplitude reductions of the order 10^3 per iteration and 10^8 overall are realisable for the feedback modelling approach. Similar levels of flow control are realisable for a multiple controller configuration. However, stationary cross-flow disturbances could not be eliminated indefinitely. Inevitably, the cross-flow instability started to grow again, albeit at a considerably lower magnitude. The analysis is extended to include the effects of systematic error in the sensors measuring capability.

I. INTRODUCTION

Control of laminar-turbulent transition on aircraft wings can potentially lead to significant drag reductions and thus reduced fuel usage; the potential lowering of operational costs and consequent lower greenhouse gas emissions from the engines is a key driver in advanced wing design. For this reason, the control of laminar boundary layers by some mechanical action, and delaying the onset of transition to locations beyond that obtained in natural unconstrained conditions has been a primary goal for the aviation industry. Laminar flow control (LFC) technologies apply modifications to the wing and surrounding flow, with control technologies classified as being passive or active. Passive control mechanisms are implemented through the careful shaping of the wing geometry, sweep or by applying steady surface suction. On the other hand, active flow control devices require an energy input and an ability to measure and adjust to variations in the flow conditions. Gad-el hak[1] describes several flow control strategies, while Joslin[2] and Arnal & Achambaud[3] review LFC applications.

The initial stage of laminar-turbulent transition is often characterised by environmental disturbances (including acoustic, vortical, and surface discontinuities[4]) that seed the growth of infinitesimally small perturbations to the laminar basic state. This process is known as receptivity[5] and establishes the initial conditions for the amplitude and phase of the instabilities that develop within the boundary layer. These can include Tollmien–Schlichting (TS) waves and cross-flow vortices. If the initial perturbation is sufficiently small, the disturbance evolution can be modelled using the linearised Navier–Stokes (LNS) equations, while nonlinear processes and the formation of secondary instabilities[6,7] must be accounted for as larger amplitudes are attained. An alternative transition route may be realised if the initial amplitude of the external disturbance (such as surface roughness) is large. Nonmodal stability theory suggests that the superposition of linearly stable non-orthogonal perturbations can lead to a short-time transient amplification of the energy contained within the initial flow conditions and establish transition to turbulence[8,9]. Numerous studies on the nonmodal mechanism for transition have been undertaken, including the flow within a duct of square cross section[10] and the flow over a flat plate[11,12]. In addition, a recent review by Kerswell[13] presents an optimisation technique based on nonlinear nonmodal analysis.

Active flow control methods can achieve a delay in transition by utilising the wave superposition principle: an unstable wave is cancelled by the excitation of an identical secondary wave with an equal amplitude but opposite phase. Leipmann and co-workers[14,15] tested this method experimentally, whereby surface mounted heated strips were used to generate and control TS waves in a water channel. It was demonstrated that unstable waves, excited by an upstream heated plate, could be almost completely eliminated by a secondary downstream heating element with an appropriate phase shift; destructive wave interference was realised. Similar levels of control of two-dimensional disturbances were observed by Thomas[16] in wind-tunnel experiments on a flat plate. However, both groups[14–16] found that the flow could never be completely relaminarised. Thomas concluded that relaminarisation was prevented by the interaction of background disturbances with the primary wave. Additionally, Thomas suggested that this particular effect could be reduced by placing the control mechanism nearer to the initial wave generator. Several further studies reported a delay in transition using

anti-phase wave control in boundary layers [17,18] and channel flows[19], while Joslin *et al*[20] report that the level of amplitude damping is sensitive to the control specifications.

Recent developments in active flow control technologies have centred around the ability to optimise the control configuration using linear control theory. Several excellent reviews on this topic[21–25] provide a detailed and informative discussion on the current and future directions for flow control. Control strategies include open-loop (or feedforward) and closed-loop (or feedback) systems, whereby control settings are either fixed or modified, respectively. Closed-loop systems require robust sensors that are capable of accurately measuring the current flow conditions. Changes in the amplitude and phase of the unstable perturbation are then relayed to the control actuator to generate an out of phase wave that cancels the initial disturbance and achieves the desired control effect. Li and Gaster[26] undertook a numerical and experimental study, whereby a row of sensors were used to measure the perturbation field and send optimal control settings downstream to an actuator that generated the required anti-phase wave. The effect of actuator and sensor location was investigated by Belson *et al*[27] using direct numerical simulations. For both feedforward (sensor upstream of control) and feedback (control upstream of sensor) systems, the relative positions of the sensor and actuator were found to determine the effectiveness of the control device.

Optimal control theory has been successfully implemented and applied to channel flows[28–30] and boundary layers[31–33]. Optimisation methods coupled with adjoint forms of the boundary layer base flow, local linear stability theory or linear parabolized stability equations[34] have been derived and used to establish conditions for attenuating disturbances subject to some cost functional constraint[35–39]. Hill[40] developed an adjoint model for determining the sensitivity of TS waves in the Blasius boundary layer. Subsequently several investigations have been undertaken to determine the sensitivity and receptivity of several boundary layer instabilities to various external forces [41–45].

Surface temperature[14,15,46,47], plasma actuators[48–50] and surface compliance[51,52] are just some of the methods that have been utilised as a means of controlling transition in boundary layers. Dynamic wall modification was utilised experimentally by Amitay *et al*[53] to excite and control TS disturbances on a flat plate. Wall modulation was implemented using piezoelectrically driven oscillating surface actuators, while the wave superposition principle was employed to attenuate disturbances. Significant cancellation of TS waves in flight experiments was also achieved by Erdmann *et al*[54], with active wave control realised using wall actuation on a laminar wing glove. An alternative control technique based on wall motion has been demonstrated by Hussein *et al*[55] for stabilising plane poiseuille flow. The surface interface was tuned to adapt to local flow pressure variations and vibrate at a desired frequency, phase and amplitude to attenuate flow disturbances. Moreover, several studies[56–60] have investigated the effects of surface roughness (coupled with free-stream turbulence) on low-pressure turbine blades, with roughness shown to establish some favourable benefits.

Voluminous works on the active control of two-dimensional and oblique TS disturbances, ranging from theoretical, numerical and experiment exist (only a few are cited above). Mughal[61] coupled a control law based on the surface shear (or pressure) linked to surface velocity perturbations using local linear stability and PSE theories. He concluded that some stabilisation could be achieved, but due to the inflectional nature of the velocity profiles and the cross-flow vortex instability being an essentially inviscid mechanism, control by near wall manipulation was more difficult.

The primary focus in LFC optimisation analyses has targeted the control of TS waves on unswept bodies and stationary cross-flow vortices excited by surface roughness on swept wings. The latter application is based on the grounds that atmospheric flight fluctuations are low enough, such that any naturally occurring unsteady cross-flow disturbances are relatively weak. Natural surface roughness on the wings of aircraft will consist of many short and long scale wavelengths of varying height and depth. Using a compressible LNS formulation Mughal and Ashworth[62] undertook an uncertainty quantification analysis of many roughness distributions based on characteristics derived from real surface measurements. Expected receptivity amplitudes were determined for varying roughness strip lengths. More recently, Thomas *et al*[45,63] applied adjoint methods to determine the mean amplitude of stationary cross-flow disturbances established by surface roughness in the flows over a swept aerofoil and a rotating disk.

The fundamental objective of this paper is to introduce a simple yet effective method for controlling linear stationary cross-flow vortices excited by surface roughness. Surface roughness and the initial amplitude of the disturbance generated by the roughness are assumed to be sufficiently small to allow nonlinear effects to be neglected. Consequently, the development and control of the stationary cross-flow disturbance are described by linear stability theory. Solutions of the LNS and adjoint linearised Navier–Stokes (ALNS) formulations are coupled to optimise the amplitude and phase of a localised wall motion that successfully brings about wave cancellation and disturbance amplitude damping. A schematic diagram of the strategy is illustrated in Fig. 1. Surface roughness excites a stationary cross-flow instability with some assumed flow conditions (Reynolds number and spanwise wavenumber), but with an unknown amplitude and phase. A sensor, located at a suitable distance downstream, measures the disturbance field and transmits the relevant information to the control mechanism. The control device is either located downstream of the sensor (feedforward model) or upstream of the sensor (feedback model). For the former strategy, the control specifications are modelled at the first attempt; cross-flow disturbances are convectively unstable and so the sensor is unable to measure the effect of the downstream control device on the disturbance development. An iterative procedure is implemented for the feedback modelling approach, whereby the sensor regularly remeasures the perturbation field and reoptimises the control conditions to achieve the greatest level of flow control. The above processes are tested on a highly unstable stationary cross-flow instability in the swept Hiemenz boundary layer. Although this particular flow is relatively sim-

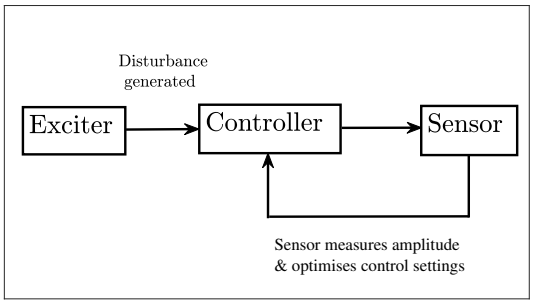


FIG. 1. Schematic diagram of the exciter-sensor-control strategy.

plistic, it has all the necessary hallmarks that are representative of more realistic aerofoil geometries.

The remainder of this paper is outlined as follows. In the subsequent section the governing equations for the swept Hiemenz flow are described. In Sec. III and Sec. IV the respective LNS and ALNS equations are presented. The sensor-control strategy is described in Sec. V and results of our investigation are discussed in Sec. VI. Finally, conclusions are given in Sec. VII.

II. UNDISTURBED FLOW

In the subsequent analysis the governing equations for the basic state and linearised disturbance development are presented in the context of the incompressible swept Hiemenz flow. However, the formulation can be easily extended to encompass other complex geometries and compressible flow systems; see the appendix of Thomas *et al*[45] for further details.

Consider the dimensional incompressible steady viscous flow $\boldsymbol{Q}(X,Y) = \{\boldsymbol{U},P\}(X,Y)$ past an infinite swept plate. Undisturbed flow fields $\boldsymbol{U} = (U,V,W)$ and P represent the steady velocity and pressure in a dimensional coordinate system $\boldsymbol{X} = (X,Y,Z)$, where the three coordinate axes X, Y and Z denote the chordwise, wall-normal and spanwise directions, respectively. Freestream flow-fields $U_\infty = mX$ (for a constant m) and W_∞ are directed along the respective X- and Z-axes, engineering the swept Hiemenz boundary layer that provides an ideal model for testing flow control technologies.

Units of length are scaled on the boundary layer thickness $\delta = \sqrt{\nu/m}$, where ν is the kinematic viscosity of the fluid. Thus, non-dimensional coordinates $\boldsymbol{x}$ are defined as

$$\boldsymbol{x} = (x,y,z) = (X,Y,Z)/\delta, \tag{1}$$

while the flow is dependent on two Reynolds numbers

$$\bar{Re} = \frac{W_\infty \delta}{\nu} \quad \text{and} \quad Re = \frac{U_\infty \delta}{\nu}, \tag{2a,b}$$

which can be used to establish the relationship

$$Re = x. \tag{3}$$

A non-dimensional base flow $\boldsymbol{Q}_B(x,y) = \{\boldsymbol{U}_B,P_B\}(x,y)$ is obtained after scaling $\boldsymbol{U}$ on U_∞:

$$U_B = \frac{U}{U_\infty} = f'(y), \tag{4a}$$

$$V_B = \frac{V}{U_\infty} = -\frac{1}{Re} f(y), \tag{4b}$$

$$W_B = \frac{W}{U_\infty} = \frac{\bar{Re}}{Re} g(y). \tag{4c}$$

Here a prime denotes differentiation with respect to y. The wall-normal functions f and g are solutions of the ordinary differential equations

$$f''' + ff'' + (1-f')^2 = 0 \tag{5a}$$

and

$$g'' + fg' = 0, \tag{5b}$$

which are solved subject to the boundary conditions

$$f = f' = g = 0 \quad \text{on} \quad y = 0 \tag{5c,d,e}$$

and

$$f' \to 1, \quad g \to 1 \quad \text{as} \quad y \to \infty. \tag{5f,g}$$

III. LINEARISED NAVIER–STOKES EQUATIONS

A. Governing equations

The unsteady incompressible LNS equations for perturbations $\boldsymbol{q} = \{\boldsymbol{u},p\}$ to the basic state $\boldsymbol{Q}_B = \{\boldsymbol{U}_B,P_B\}$ are given as

$$\mathscr{L}(\boldsymbol{U_B},\boldsymbol{q}) = 0, \quad \nabla\cdot\boldsymbol{u} = 0, \tag{6a,b}$$

for

$$\mathscr{L}(\boldsymbol{U}_B,\boldsymbol{q}) = \frac{\partial \boldsymbol{u}}{\partial t} + (\boldsymbol{U}_B\cdot\nabla)\boldsymbol{u} + (\boldsymbol{u}\cdot\nabla)\boldsymbol{U}_B + \nabla p - \frac{1}{Re}\nabla^2\boldsymbol{u}. \tag{6c}$$

Stationary cross-flow perturbations $\boldsymbol{q}$ are assumed to be linear, infinitesimally small and of the general form

$$\boldsymbol{q}(\boldsymbol{x},t) = \hat{\boldsymbol{q}}(x,y)e^{i(\beta z-\omega t)} + \text{c.c.}, \tag{7}$$

where β and ω (set to zero for the current study) denote the periodic spanwise wavenumber and frequency, respectively. Here $\hat{\boldsymbol{q}} = \hat{\boldsymbol{q}}(x,y)$ encompasses the amplitude and spatial evolution of the disturbance and c.c. denotes the complex conjugate.

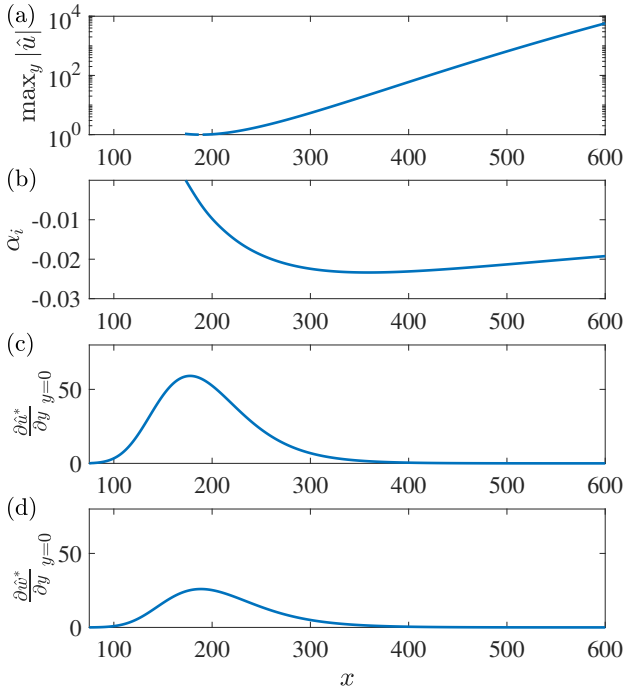


FIG. 2. Perturbation fields corresponding to the stationary cross-flow instability established for parameter settings $\bar{R}e = 500$ and $\beta = 0.4$. (a) Maximum absolute value of the $\hat{u}$-velocity. (b) Chordwise growth rate α_i. (c,d) Absolute value of the normalised adjoint perturbation fields $\partial\hat{u}^*/\partial y$ and $\partial\hat{w}^*/\partial y$, on the plate surface $y = 0$.

The spatial development of the disturbance $\hat{\boldsymbol{q}}$ is assumed to be of the general form

$$\hat{\boldsymbol{q}}(x,y) = A\tilde{\boldsymbol{q}}(x,y), \tag{8}$$

where $\tilde{\boldsymbol{q}}$ describes the evolution and growth of the perturbation that is dependent on the initial flow settings (i.e. $\bar{R}e$ and β). For the subsequent study $\tilde{\boldsymbol{q}}$ is assumed to be of the form

$$\tilde{\boldsymbol{q}}(x,y) = \tilde{\tilde{\boldsymbol{q}}}(x,y)\exp\int_{x_0}^{x}\alpha(s)\,\mathrm{d}s, \tag{9}$$

for a complex chordwise wavenumber $\alpha = \alpha_r + i\alpha_i$ and a slowly varying shape function $\tilde{\tilde{\boldsymbol{q}}}$. Here x_0 denotes the chord location that the cross-flow instability first becomes linearly unstable. The disturbance amplitude is then represented by the (possibly complex) constant A that is governed by the shape, form and location of the initial forcing. Here the initial forcing is prescribed by the boundary condition $\boldsymbol{u}_w$ defined below in Sec. III.B.

Figure 2(a,b) illustrates the maximum absolute value of the $\tilde{u}$-velocity perturbation field (normalised to unity about $x = x_0 \equiv 187$) and the chordwise growth rate α_i, as a function of the chordwise x-direction, for the Reynolds number $\bar{R}e = 500$ and spanwise wavenumber $\beta = 0.4$.

B. Boundary conditions

No-slip and Dirichlet boundary conditions are imposed on the surface and in the far-field limit

$$\boldsymbol{u} = 0 \quad \text{on} \quad y = 0 \quad \text{and} \quad \boldsymbol{u} \to 0 \quad \text{as} \quad y \to \infty. \tag{10a,b}$$

Stationary cross-flow vortices are then excited by a surface roughness distribution and controlled via a surface fluctuation that are both implemented through a linearisation of the no-slip boundary condition

$$\boldsymbol{u} = \boldsymbol{u}_w \quad \text{on} \quad y = 0, \tag{11a}$$

where $\boldsymbol{u}_w = (u_w, v_w, w_w)$ represents the surface condition that is decomposed into an upstream exciter $\boldsymbol{u}_e$ and a downstream control condition $\boldsymbol{u}_c$

$$\boldsymbol{u}_w = \boldsymbol{u}_e + \boldsymbol{u}_c. \tag{11b}$$

1. *Surface roughness*

Stationary cross-flow disturbances are excited by setting the boundary condition (11) for $\boldsymbol{u}_e = (u_e, v_e, w_w)$ as

$$u_e = -h_e U_B'(0)\mathrm{e}^{i\beta z} + \text{c.c.}, \tag{12a}$$
$$w_e = -h_e W_B'(0)\mathrm{e}^{i\beta z} + \text{c.c.}, \tag{12b}$$
$$v_e = 0, \tag{12c}$$

where the surface roughness distribution is modelled as

$$h_e(x) = \sum_{j=1}^{N} b_j \cos\left(2\pi\left(\frac{jx}{x_{\text{len}}} + \kappa_j\right)\right). \tag{12d}$$

Here N is a short scale wavelength filter, x_{len} denotes a streamwise wavelength, and b_j and κ_j represent randomly generated roughness amplitudes and phase shifts, respectively.

The roughness distribution used throughout the following study is modelled on the finite chord interval $x_{\text{in}} \le x \le x_{\text{out}}$, with $x_{\text{len}} = x_{\text{out}} - x_{\text{in}}$. Moreover, each amplitude b_j is scaled by the factor

$$\left(\frac{x_{\text{len}}}{2\pi j}\right)^k, \tag{13}$$

for a power law coefficient k. This approach for modelling surface roughness is implemented following the observations of earlier studies[64–67] that demonstrated the power spectral density (PSD) for natural surface roughness follows a power law of the form (13). For instance, Van Deusen[64] showed that PSD reduced with the square of the angular frequency for many surfaces, while Mughal and Ashworth[62] observed that the PSD of a painted and unpainted plate were greater in the longer roughness wavelengths. More recently, Raposo et al.[68] and Thomas and Davies[63] utilised this approach for modelling surface roughness in their respective receptivity investigations

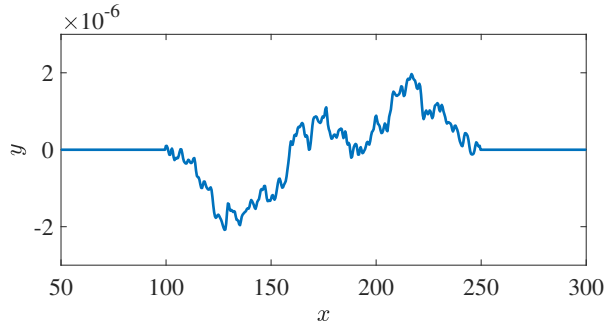


FIG. 3. Surface roughness distribution used in this study.

and set the power law coefficient $k = 1$ to ensure the PSD decayed at the rate found by Van Deusen[64]. Finally, the roughness distribution h_e is scaled on the root-mean-square (rms)

$$h_{e,\mathrm{rms}} = \sqrt{\frac{1}{x_{\mathrm{len}}}\int_{x_{\mathrm{in}}}^{x_{\mathrm{out}}} h_e^2 \,\mathrm{d}x}. \tag{14}$$

In the following analysis $N = 200$ was sufficient to generate a roughness strip encompassing a broad range of length scales. Moreover, since receptivity is enhanced by roughness elements located near the chord region that the stationary cross-flow instability first becomes unstable[69] ($x_0 \approx 187$ for $\bar{R}e = 500$ and $\beta = 0.4$), the roughness distribution modelled throughout this study was fixed about the chord interval $100 \leq x \leq 250$, i.e. $x_{\mathrm{len}} = 150$. Additionally, the power law coefficient and rms were set as $k = 1$ and $h_{e,\mathrm{rms}} = 10^{-6}$, respectively. Figure 3 illustrates the surface roughness used in the subsequent investigation.

2. *Control mechanism*

Control of the stationary cross-flow vortex (established by the surface roughness) is realised using a model for localised wall motion, whereby the boundary condition $\boldsymbol{u}_c = (u_c, v_c, w_c)$ in (11) is defined as

$$u_c = -h_c U_B'(0) e^{i\beta z} + \mathrm{c.c.}, \tag{15a}$$
$$w_c = -h_c W_B'(0) e^{i\beta z} + \mathrm{c.c.}, \tag{15b}$$
$$v_c = 0, \tag{15c}$$

for a chordwise distribution

$$h_c(x; x_c, \lambda) = a_n e^{i\phi_n} \cos\left((x - x_c)\,\pi/\lambda\right) \tag{15d}$$

on $-\lambda/2 \leq x - x_c \leq \lambda/2$ and zero elsewhere. The control device is centred about a chord position x_c with a fixed chord length λ. The parameters a_n and ϕ_n denote the respective amplitude and phase shift of the control mechanism that are to be optimised, while the subscript n denotes the iteration number in the sensor-control iterative procedure described below in Sec. V.

IV. ADJOINT LINEARISED NAVIER–STOKES EQUATIONS

A. Governing equations

The ALNS equations are derived from the Lagrange identity, which is formulated by applying integration by parts to the scalar product of the LNS Eqs. (6) with the adjoint perturbation fields $\boldsymbol{q}^* = \{\boldsymbol{u}^*, p^*\}$

$$\left[\mathscr{L}(\boldsymbol{U}_B, \boldsymbol{q}) \cdot \boldsymbol{u}^* + \nabla \cdot \boldsymbol{u} p^*\right] + \left[\boldsymbol{u} \cdot \mathscr{L}^*(\boldsymbol{U}_B, \boldsymbol{q}^*) + p \nabla \cdot \boldsymbol{u}^*\right] = \frac{\partial K_t}{\partial t} + \nabla \cdot (K_x, K_y, K_z). \tag{16}$$

The ALNS system of equations are then defined as

$$\mathscr{L}^*(\boldsymbol{U}_B, \boldsymbol{q}^*) = 0, \quad \nabla \cdot \boldsymbol{u}^* = 0, \tag{17a,b}$$

where

$$\mathscr{L}^*(\boldsymbol{U}_B, \boldsymbol{q}^*) = \frac{\partial \boldsymbol{u}^*}{\partial t} + (\boldsymbol{U}_B \cdot \nabla)\boldsymbol{u}^* - (\nabla \boldsymbol{U}_B)^{\mathsf{T}} \boldsymbol{u}^* + \nabla p^* + \frac{1}{Re}\nabla^2 \boldsymbol{u}^*, \tag{17c}$$

for adjoint perturbation fields of the form

$$\boldsymbol{q}^*(\boldsymbol{x}, t) = \hat{\boldsymbol{q}}^*(x, y) e^{-i(\beta z - \omega t)} + \mathrm{c.c.} \tag{18}$$

A change in sign arises for both ω and β as adjoint disturbances evolve both backwards in time and in the spatially opposite sense to the LNS perturbation (7).

The operator $\boldsymbol{K} = (K_t, K_x, K_y, K_z)$ on the right-hand-side of the Lagrange identity (16) represents the bi-linear concomitant and is defined as

$$K_t = \boldsymbol{u} \cdot \boldsymbol{u}^*, \tag{19a}$$

$$K_x = U_B \boldsymbol{u} \cdot \boldsymbol{u}^* + p u^* + u p^* + \frac{1}{\bar{R}e}\left(u\frac{\partial u^*}{\partial x} - u^*\frac{\partial u}{\partial x} + v\frac{\partial v^*}{\partial x} - v^*\frac{\partial v}{\partial x} + w\frac{\partial w^*}{\partial x} - w^*\frac{\partial w}{\partial x}\right), \tag{19b}$$

$$K_y = V_B \boldsymbol{u} \cdot \boldsymbol{u}^* + p v^* + v p^* + \frac{1}{\bar{R}e}\left(u\frac{\partial u^*}{\partial y} - u^*\frac{\partial u}{\partial y} + v\frac{\partial v^*}{\partial y} - v^*\frac{\partial v}{\partial y} + w\frac{\partial w^*}{\partial y} - w^*\frac{\partial w}{\partial y}\right), \tag{19c}$$

$$K_z = W_B \boldsymbol{u} \cdot \boldsymbol{u}^* + p w^* + w p^* + \frac{1}{\bar{R}e}\left(u\frac{\partial u^*}{\partial z} - u^*\frac{\partial u}{\partial z} + v\frac{\partial v^*}{\partial z} - v^*\frac{\partial v}{\partial z} + w\frac{\partial w^*}{\partial z} - w^*\frac{\partial w}{\partial z}\right), \tag{19d}$$

for

$$\boldsymbol{u} \cdot \boldsymbol{u}^* = u u^* + v v^* + w w^*.$$

In the subsequent analysis the $\boldsymbol{K}$-operator will be utilised to establish a formula for predicting the control specifications required to dampen the stationary cross-flow vortex established by surface roughness.

B. Normalisation

Assuming Fourier modes $\boldsymbol{q}$ and $\boldsymbol{q}^*$ (given by Eqs. (7) and (18)) are distinct modes of the respective systems (6) and (17), the Lagrange identity (16) can be reduced to the form

$$\frac{\partial K_x}{\partial x} + \frac{\partial K_y}{\partial y} = 0, \tag{20}$$

where K_x and K_y are given explicitly in terms of $\hat{\boldsymbol{q}}$ and $\hat{\boldsymbol{q}}^*$. Furthermore, Eq. (20) can be simplified by integrating over the (x,y) domain, for $y \in [0:\infty)$ and $x \in [x_1:x_2]$, to give

$$\mathscr{K}(x) = \int_{y=0}^{\infty} K_x(\hat{\boldsymbol{q}}, \hat{\boldsymbol{q}}^*)\,\mathrm{d}y, \tag{21}$$

where the usual homogeneous boundary conditions are implemented on the surface and in the farfield. The quantity $\mathscr{K}$, given by Eq. (21), is fundamental to normalising disturbances and utilising the adjoint approach for optimising laminar flow control.

Linear perturbations $\hat{\boldsymbol{q}}$ are normalised by setting

$$\max|\hat{u}(x,y)| = 1 \quad \text{at} \quad x = x_0, \tag{22a}$$

while adjoint perturbation fields $\hat{\boldsymbol{q}}^*$ are normalised by setting

$$\mathscr{K} = 1 \;\forall\, x. \tag{22b}$$

C. Adjoint amplitude formula

The amplitude A of the stationary cross-flow instability may be computed by rearranging Eq. (8) as

$$A = \hat{\boldsymbol{q}}/\tilde{\boldsymbol{q}},$$

with $\tilde{\boldsymbol{q}}$ given by Eq. (9). Alternatively, the amplitude A of the linear perturbation $\hat{\boldsymbol{q}}$ can be computed by coupling (8) with the Lagrange identity (16) and boundary conditions (11). On integrating over the wall-normal direction $y \in [0,\infty)$ and the streamwise interval $x \in [x_1, x_2]$, the following formula for the amplitude A of the linear disturbance is derived

$$A = \int_{x_1}^{x_2} K_y(\hat{\boldsymbol{q}}, \hat{\boldsymbol{q}}^*)|_{y=0}\,\mathrm{d}x, \tag{23a}$$

for

$$K_y = v_w \hat{p}^* + \frac{1}{\bar{R}e}\left(u_w \frac{\partial \hat{u}^*}{\partial y} + w_w \frac{\partial \hat{w}^*}{\partial y}\right). \tag{23b}$$

Here x_1 and x_2 are streamwise locations sufficiently far upstream and downstream of the boundary condition $\boldsymbol{u}_w$. Thus, the amplitude A of the linear cross-flow instability may be determined using only the form of the wall condition $\boldsymbol{u}_w$ and the adjoint solution $\hat{\boldsymbol{q}}^*$ to the system of Eqs. (17). For instance, amplitudes $A_{c,n}$ established by the control device (15) are given as

$$\begin{aligned} A_{c,n} &= \int_{x_1}^{x_2} h_c(x) f_c(x)\,\mathrm{d}x, \\ &= a_n \mathrm{e}^{i\phi_n} I, \end{aligned} \tag{24a}$$

for

$$I = \int_{x_1}^{x_2} \cos\left((x - x_c)\,\pi/\lambda\right) f_c(x)\,\mathrm{d}x \tag{24b}$$

and

$$f_c(x) = -\frac{1}{\bar{R}e}\left(U_B'(0)\frac{\partial \hat{u}^*}{\partial y} + W_B'(0)\frac{\partial \hat{w}^*}{\partial y}\right)\bigg|_{y=0}. \tag{24c}$$

(Subscripts n again reference the iteration number in the sensor-control procedure described below in Sec. V.) In the subsequent analysis, the adjoint formula (24) is used to predict the complex-valued integral I. Adjoint computations are then coupled to sensor measurements of the stationary cross-flow instability (established by surface roughness) to optimise the control amplitude a_n and phase shift ϕ_n required to establish an anti-phase wave that brings about destructive wave interference.

Figure 2(c,d) displays the absolute value of the normalised adjoint perturbation fields $\partial\hat{u}^*/\partial y$ and $\partial\hat{w}^*/\partial y$ on the plate surface $y = 0$, in the instance $\bar{R}e = 500$ and $\beta = 0.4$, which are required in the adjoint integral Eqs. (23)-(24). Both quantities are greatest about the chord interval that the cross-flow instability first becomes unstable (i.e., $x_0 \approx 187$), and consequently receptivity is enhanced by roughness elements located in this region[69].

D. Numerical method

Harmonic forms of both the LNS and ALNS systems of equations are discretised and solved in the manner described by Mughal[70]. Fourth-order finite difference methods with $N_x = 2001$ points are used along the chordwise x-axis, while a pseudo-spectral approach is utilised in the wall normal y-direction. Additionally, a stretched wall-normal grid is implemented that ensures points are concentrated within the boundary layer. This is achieved by mapping the semi-infinite physical domain $y \in [0,\infty)$ onto the finite computational interval $\eta \in [0,1)$ via the coordinate transformation

$$\eta = \frac{y}{c+y}, \tag{25}$$

where the constant c is chosen to ensure points are clustered about $y = 1$. High resolution solutions are then obtained for $N_y = 51$ spectral points; calculations presented herein are not noticeably improved by considering a larger number of N_y-points. Ultimately, discretisation of the two formulations leads to requiring the inversion of large sparsely banded matrices

$$\mathsf{P}\boldsymbol{q} = \boldsymbol{r}, \tag{26}$$

where $\boldsymbol{r}$ comprises the boundary conditions (10)-(15). Solutions $\boldsymbol{q}$ are then obtained following a standard lower-upper factorisation for the inversion of P.

V. CONTROL STRATEGY

The successful control of stationary cross-flow disturbances is realised using the exciter-sensor-control strategy depicted in Fig. 1 that is based on the following iterative procedure.

1. Coupled together surface roughness (12) and the control mechanism (15) establish a stationary cross-flow instability

$$\hat{\boldsymbol{q}}_n = \hat{\boldsymbol{q}}_e + \hat{\boldsymbol{q}}_{c,n},$$

for a given Reynolds number $\bar{R}e$ and spanwise wavenumber β, but with an unknown amplitude. Here $\hat{\boldsymbol{q}}_e$ represents the stationary cross-flow instability excited by the surface roughness, while the equivalent disturbance generated by the control mechanism $\hat{\boldsymbol{q}}_{c,n}$ is assumed to be of the form (8) with an amplitude given by (24)

$$\hat{\boldsymbol{q}}_{c,n}(x,y) = a_n \mathrm{e}^{i\phi_n} I\tilde{\boldsymbol{q}}(x,y). \tag{27}$$

The spatial growth $\tilde{\boldsymbol{q}} = \tilde{\boldsymbol{q}}(x,y)$ is of the form (9) and the complex-valued integral I is given by (24b). The subscript n denotes the iteration number in the sensor-control process. For instance, $n = 0$ corresponds to the situation where the control device is switched off (i.e., $\tilde{\boldsymbol{q}}_0 = \tilde{\boldsymbol{q}}_e$ and $a_n = \phi_n = 0$), whereas $n > 0$ represents the case where the control device is turned on and configured after n iterations. (It is worth emphasising here that only the linear perturbation generated by the control mechanism, $\hat{\boldsymbol{q}}_{c,n}$, is assumed to be of the form (8). No such assumption is made about those disturbances excited by the surface roughness, $\hat{\boldsymbol{q}}_e$, nor established by coupling the controller with the roughness, $\hat{\boldsymbol{q}}_n$.)

2. A sensor measures the disturbance $\hat{\boldsymbol{q}}_n$ about some fixed spatial position $(x,y) = (x_s, y_s)$. For the subsequent study, calculations are based on the pressure perturbation field $\hat{p}$ and shear stress $\partial\hat{u}/\partial y$ at the wall: $y_s = 0$. However, the method could easily be adapted to other disturbance characteristics and comparable results would be realised.

3. The sensor relays the disturbance measurements to the control device, with the aim to configure the control amplitude a_n and phase shift ϕ_n to optimise disturbance attenuation (recall Eqs. (15) and (24)); the control mechanism generates an anti-phase wave that dampens the wave established by the surface roughness. This is achieved by setting

$$\hat{\boldsymbol{q}}_{c,n}(x_s, y_s) = -\hat{\boldsymbol{q}}_{n-1}(x_s, y_s),$$

with optimal a_n and ϕ_n settings given by

$$a_n = \sqrt{\psi_{r,n}^2 + \psi_{i,n}^2}, \tag{28a}$$

and

$$\phi_n = \arctan\left(\frac{\psi_{i,n}}{\psi_{r,n}}\right), \tag{28b}$$

for

$$\psi_n \equiv \psi_{r,n} + i\psi_{i,n} = -\frac{\hat{\boldsymbol{q}}_{n-1}(x_s, y_s)}{I\tilde{\boldsymbol{q}}(x_s, y_s)}. \tag{28c}$$

4. If the sensor is located upstream of the control device (feedforward modelling approach) the iterative procedure is stopped after the first iteration. Further iterations will not bring about any additional control benefits as the sensor is unable to perceive downstream changes to the disturbance development brought about by the control device; stationary cross-flow disturbances are convective. On the other hand, if the sensor is located downstream of the control mechanism (feedback system), the iterative process is repeated until the control settings are optimised and are unable to engineer any further reductions in the amplitude of the cross-flow vortex.

5. The success of the control strategy, in modulating the size of the stationary cross-flow disturbance, is then measured by comparing the perturbation amplitudes established by the surface roughness without and with the application of the control mechanism. The amplitude ratio

$$\gamma = \left|\frac{\hat{\boldsymbol{q}}_n(x_s, y_s)}{\hat{\boldsymbol{q}}_0(x_s, y_s)}\right|, \tag{29}$$

can then be utilised to give a measure of the control success after the nth iteration. Amplitudes $\gamma < 1$ correspond to a favorable control effect with a reduction in the disturbance amplitude realised.

VI. RESULTS

For the subsequent analysis we limit our study to the stationary cross-flow instability established for the parameter settings $(\bar{R}e, \beta) = (500, 0.4)$. These particular parameters were chosen as they correspond to a highly unstable perturbation and provide an excellent test case for illustrating the sensor-control strategy. Moreover, the same parameter settings were utilised in a number of previous works[71,72].

A. One controller

1. *Test case*

Before undertaking a study of the sensor and control location, and measuring capability, we first illustrate the control strategy for a test feedback system. The surface roughness, plotted in Fig. 3, establishes a stationary cross-flow vortex matching the above parameter settings. The blue solid curves in Fig. 4 depict the resulting maximum absolute values of the u-velocity and pressure p perturbation fields as a function of the chordwise x-direction. Downstream of the surface roughness, the stationary cross-flow instability grows rapidly. (The

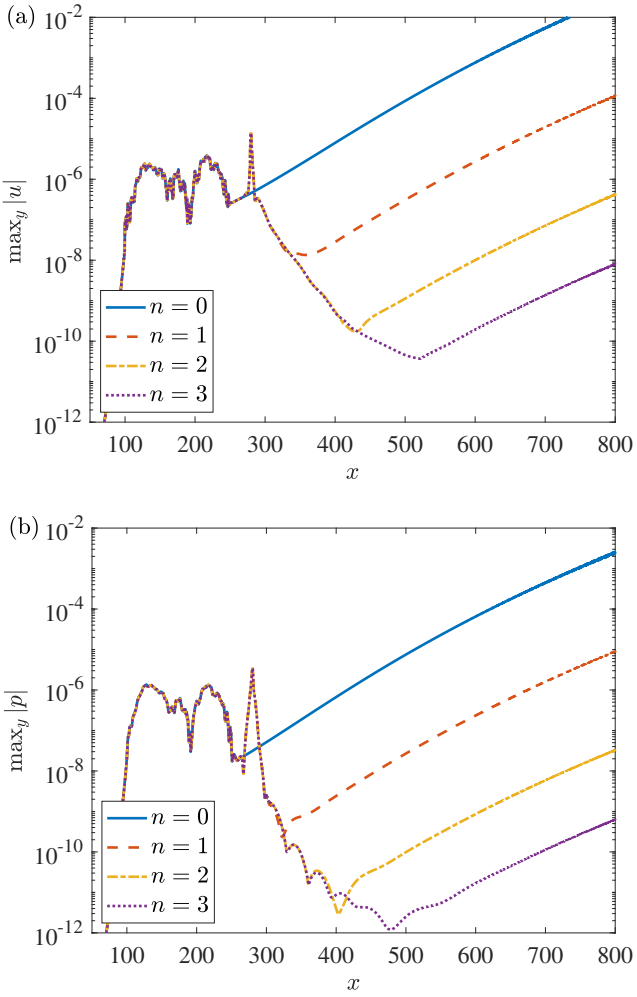


FIG. 4. Maximum absolute value of (a) the u-velocity and (b) the pressure p perturbation fields for a stationary cross-flow instability established for the parameter settings $\{\bar{R}e, \beta\} = \{500, 0.4\}$. Perturbation excited by the surface roughness given in Fig. 3, with a control device centred about $x_c = 280$ and a sensor fixed at $x_s = 480$.

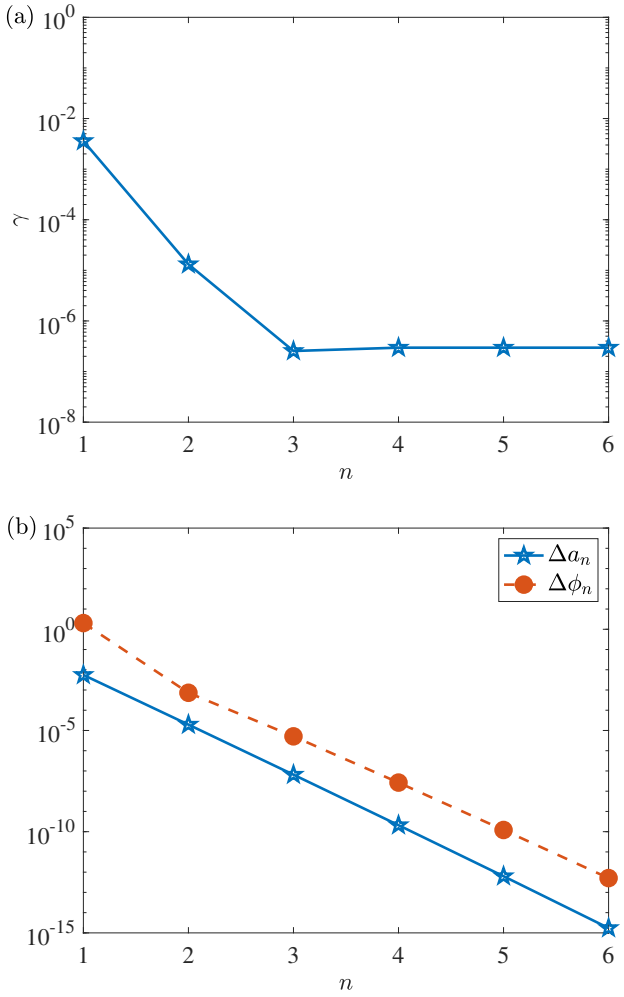


FIG. 5. (a) Amplitude ratio γ and (b) variation in $(\Delta a_n, \Delta \phi_n)$, as a function of the number of iterations n, for the stationary cross-flow instability depicted in Fig. 4.

hat notation has been dropped here and in the subsequent discussion for simplicity.) A sensor, without any internal error and located about $x_s = 480$, measures the local disturbance field $\boldsymbol{q}_0$. (For this example, measurements are based on the wall pressure perturbation field p.) Measurements are then relayed to a control mechanism centred about $x_c = 280$ with a fixed chord length $\lambda = \pi$. (Note that no special significance should be attached to the chosen value for λ. This particular length setting was simply chosen to illustrate the control optimisation strategy and similar behaviour was realised for other λ values.) The adjoint amplitude formula, given by Eq. (24), is then used to compute the complex-valued integral I. Coupling the solution for I with Eqs. (24) and (28), the control amplitude a_1 and phase shift ϕ_1 (corresponding to the first iteration in the sensor-control process) are configured to optimise attenuation of the cross-flow instability. The control device generates a stationary cross-flow disturbance that is approximately the anti-phase wave of that initially excited by the surface roughness. The maximum absolute value of u and p, that encompasses both the surface roughness and the control device after one iteration, are illustrated by the red dashed curves in Fig. 4. There is a clear and marked reduction in the disturbance amplitude; the amplitude of the cross-flow vortex has decreased by approximately two to three orders of magnitude. Figure 5(a) depicts the corresponding amplitude ratio γ as a function of the number of iterations n. The illustration indicates that γ is of the order 10^{-3} to 10^{-2} after only one iteration. Hence, a considerable level of LFC has been achieved.

Due to minor numerical inaccuracies brought about by the computational approach or as a consequence of near field effects and in assuming that the perturbation excited by the control device is of the form (27), the control mechanism fails to generate an exact anti-phase wave that fully negates the development of the stationary cross-flow instability. (It is worth noting that increasing the number of points N_x and N_y along

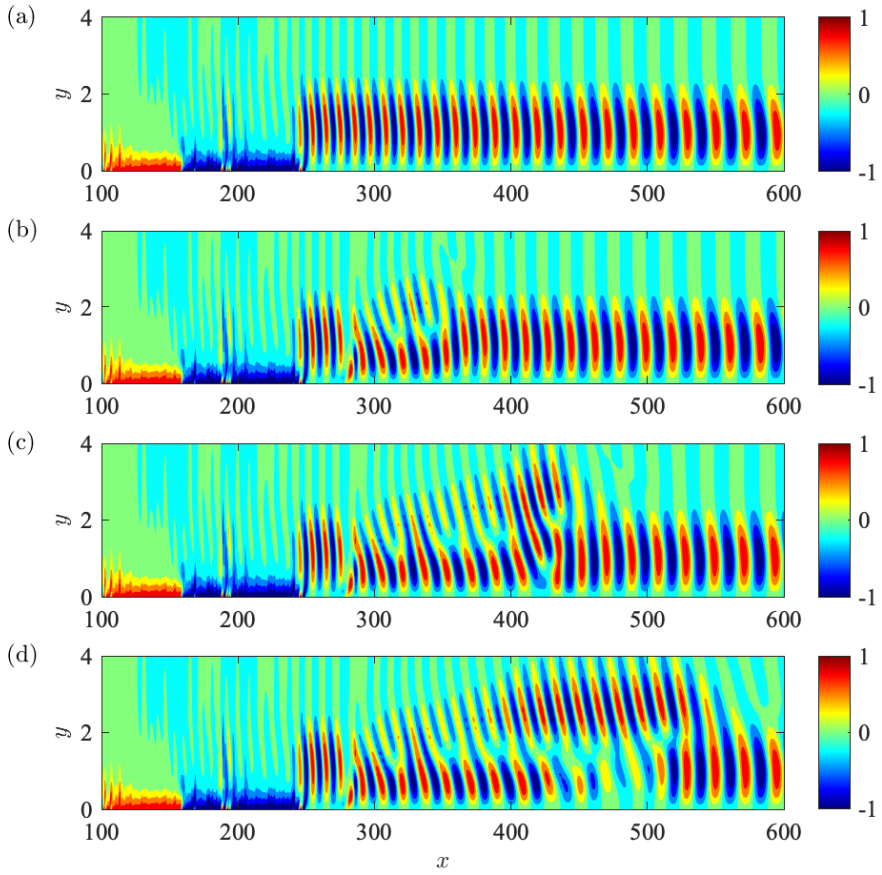


FIG. 6. Disturbance development $u/\max_y|u|$ in the (x,y)-plane, corresponding to the stationary cross-flow instability modelled in Fig. 4. Solution with the control device configured after n iterations. (a) $n=0$, (b) $n=1$, (c) $n=2$, and (d) $n=3$.

the respective x- and y-directions did not affect this particular result.) However, further amplitude reductions were realised by making minor modifications to the control specifications. This was achieved by making new perturbation measurements and by reconfiguring the control settings for the localised wall motion. The sensor remeasures the stationary cross-flow disturbance (now labelled $\boldsymbol{q}_1$), and the control device employs the iterative scheme described in Sec. V (recall Eq. (28)) to correct and re-optimise the control amplitude and phase shift (now labelled a_2 and ϕ_2, respectively). The yellow chain curves in Fig. 4 depict those solutions obtained following the second iteration of the sensor-control procedure. The amplitude of the cross-flow instability has been reduced by a further two to three orders of magnitude, with $\gamma \sim O(10^{-5})$ for $n=2$, as shown in Fig. 5(a).

A third iteration establishes a further reduction in the cross-flow vortex amplitude (purple dotted curve in Fig. 4) with γ now of the order 10^{-7}. However, further iterations were not found to bring about any additional control benefits. This is primarily due to the perturbation attaining a minimum value about the sensor location and the appearance of small numerical fluctuations brought about by the computational precision. Figure 5(a) indicates that the parameter γ achieves a minimum value of $O(10^{-7})$ after only three iterations. Although this is only specifically true for the exciter-sensor-control system modelled in Fig. 4, similar levels of flow control were realised for other roughness distributions and sensor-control arrangements.

The corresponding variations in the optimal control amplitude a_n and phase shift ϕ_n are respectively defined as

$$\Delta a_n = a_n - a_{n-1} \qquad \text{and} \qquad \Delta\phi_n = \phi_n - \phi_{n-1},$$

and plotted in Fig. 5(b) for the first six iterations. Both Δa_n and $\Delta\phi_n$ decrease significantly after each iteration, eventually achieving values of the order 10^{-8} and less. Thus, the control settings quickly converge towards the optimal 'sweet-spot'.

Figure 6 displays contours of the u-velocity disturbance development in the (x,y)-plane for those stationary cross-flow instabilities modelled in Fig. 4. The upper illustration depicts the stationary cross-flow disturbance established by the surface roughness, while the remaining three illustrations depict the solutions following the application of the control device after $n=1$, $n=2$, and $n=3$ iterations. In all instances, the disturbance evolution has been normalised on the local maximum

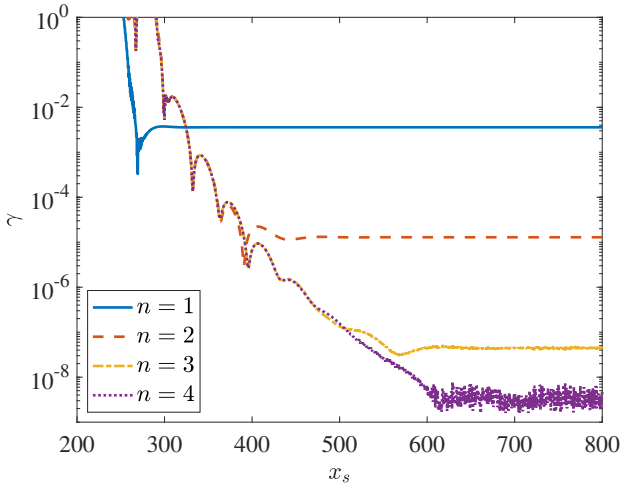


FIG. 7. Amplitude ratio γ as a function of the sensor location x_s, corresponding to the stationary cross-flow instability modelled in Fig. 4.

absolute value of the u-velocity perturbation field, $\max_y |u|$. It is worth emphasising that the magnitude of the cross-flow instability is significantly reduced downstream of the control mechanism and that the normalisation has been implemented to ensure that disturbance characteristics and the response to the control device are visible across the entire spatial domain. (The large spatial growth associated with the cross-flow instability would otherwise make this impossible.) Red and blue contours depict the positive and negative valued u-levels, respectively. As expected, in the absence of the control mechanism, the cross-flow instability develops near the planar surface. However, once the control device has been switched on and the optimal settings configured, the controlled disturbance splits into two separate components, an upper and lower part, over the interval that the control device modulates the flow. As the number of iterations n increases, the control settings converge towards the optimal 'sweet spot' and the control device has a greater influence on the local disturbance development. Eventually, downstream of the sensor ($x_s = 480$), the two components recoalesce and the disturbance evolution is once again characterised by the typical cross-flow mode structure. Beyond this location the stationary cross-flow instability again develops and grows, albeit at a significantly smaller magnitude. This particular characteristic coincides with the location that a minimum was observed in those plots depicted in Fig. 4.

2. *Effect of sensor location*

The effect of the sensor location x_s on the control mechanisms ability to attenuate the amplitude of the stationary cross-flow vortex is considered in Fig. 7. The stationary cross-flow disturbance was again excited by the surface roughness plotted in Fig. 3, while the control mechanism was fixed about the chord position $x_c = 280$. Sensor measurements were again based on the pressure p perturbation field at the wall, while the sensor location x_s was varied. The size of the amplitude ratio γ, after the first four iterations, was computed and plotted as a function of the sensor location x_s. Very little control benefits were realised for a sensor located in the chord region immediately downstream of the roughness and control device. Indeed some adverse flow control conditions were configured in the immediate vicinity of the control mechanism for iterations $n \geq 2$. Nevertheless, considerable favorable flow control conditions were found for a sensor located sufficiently far downstream. After each successive iteration, the greatest level of amplitude damping was achieved for a sensor located about $x_s \approx 290$, 450, 590 and 600. (Each of these locations corresponds to a sensor fixed at least 10, 170, 310 and 320 chord units downstream of the control device centre $x_c = 280$.) Furthermore, for each iteration n, the size of γ was unchanged by increasing the sensor location x_s to larger chord positions. Thus, there appears to be an optimal sensor-control distance, $x_s - x_c$, required to establish the greatest level of LFC.

Amplitude reductions γ of the order 10^{-8} were achieved after $n = 4$ iterations for a sensor located about $x_s \approx 600$. Additional iterations were not found to bring about any further flow control advantages. Indeed for $x_s > 600$ and $n = 4$, the size of γ fluctuates about 10^{-8}, which suggests that numerical inaccuracies brought about by round-off errors have become significant and prevent further LFC benefits at larger iterations n and sensor locations x_s.

For the iteration number $n = 4$ and sensors centred about the chord interval $x_s \in [300, 600]$, the size of γ was found to decrease at an exponential rate. Similar trends were observed for other flow control specifications (that is, variable x_c and λ). Moreover, it is worth noting that for sensors located very near the control device (that is, $x_s \approx x_c$), the size of γ obtained after one iteration is less than that realised after $n \geq 2$ iterations. Thus, if the sensor is located very near the control mechanism, it is preferable to apply the iterative procedure only once. Hence, a feedforward modelling approach is the most suitable control method in this instance.

3. *Feedforward modelling*

We now consider a feedforward sensor-control arrangement, where the control device is always located downstream of the sensor. Providing this particular requirement was met, the location of the control mechanism was not found to affect the subsequent analysis. Additionally, control settings were configured after only one iteration for the reasons discussed in Sec. V.

Figure 8 displays the size of γ obtained after one iteration: $\gamma_{n=1}$. Results are plotted as a function of the sensor location x_s, with sensor measurements based on the wall pressure p (solid blue curves) and wall shear stress $\partial u/\partial y$ (dashed red). Amplitude reductions of the order 10^{-3} are realised, providing the sensor is located approximately 40 chord units downstream of the roughness strip (which ends at $x = 250$ for the example modelled). Calculations are only marginally affected by the disturbance quantity measured by the sensor, with identical control benefits realised for sufficiently large sensor loca-

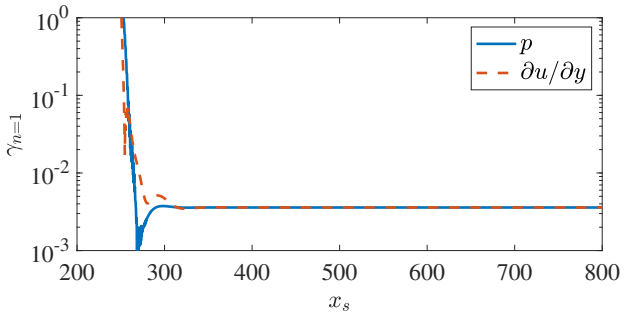


FIG. 8. Amplitude ratio $\gamma_{n=1}$ obtained after one iteration as a function of the sensor location x_s, for a feedforward system, where the sensor measurements are based on the wall pressure p (solid lines) and wall shear stress $\partial u/\partial y$ (dashed). Roughness and control settings match those conditions modelled in Fig. 4.

tions x_s. Measuring the wall pressure perturbation field proves to be marginally more efficient in the chord range immediately downstream of the surface roughness, than equivalent calculations based on measurements of the wall shear stress. However, this particular observation is likely a consequence of the numerical strategies implemented herein as opposed to some unknown physical phenomena.

4. *Feedback modelling*

A feedback sensor-control system is constructed when the sensor is located downstream of the control device. Thus, the disturbance field can be continually remeasured and the control settings re-optimised. Figure 9 displays the minimum value of the amplitude ratio γ, denoted $\gamma_{\min}$, as a function of the sensor-control distance $x_s - x_c$. Results are again presented for the surface roughness modelled in Fig. 4 and a control device centred about three monotonically increasing chord locations: $x_c = 280$ (blue solid lines), $x_c = 373$ (red dashed) and $x_c = 466$ (yellow chain). The amplitude ratio $\gamma_{\min}$ is based on those solutions obtained after $n = 4$ iterations, as further iterations were not found to bring about any additional control benefits for the roughness and control specifications modelled. Solutions in Fig. 9(a) correspond to measurements based on the pressure p perturbation field at the wall, while those results depicted in Fig. 9(b) are based on measurements of the wall shear stress $\partial u/\partial y$. The dotted black line depicts the equivalent γ-computations obtained after one iteration that corresponds to those results obtained using the feedforward modelling approach.

Amplitude reductions $\gamma_{\min}$ were marginally affected by the location x_c of the control mechanism. The local wall motion centred about $x_c = 280$ establishes greater amplitude reductions at smaller distances $x_s - x_c$, compared to those control devices centred about $x_c = 373$ and $x_c = 466$. Fixing the control device (and by extension the sensor) nearer to the roughness strip limits the initial growth of the stationary cross-flow instability (established by the roughness) to only moderate amplitudes. Whereas a control device located further downstream has to overcome significantly larger amplitudes, as the disturbance has had a greater chord range to grow. Furthermore, as discussed above, receptivity is enhanced by roughness or other types of forcing (such as the control device) in the chord region that the cross-flow disturbance first becomes linearly unstable[69]. Thus, we might expect the control-optimisation strategy to be most affected by a control device located in the chord region that the cross-flow instability first emerges.

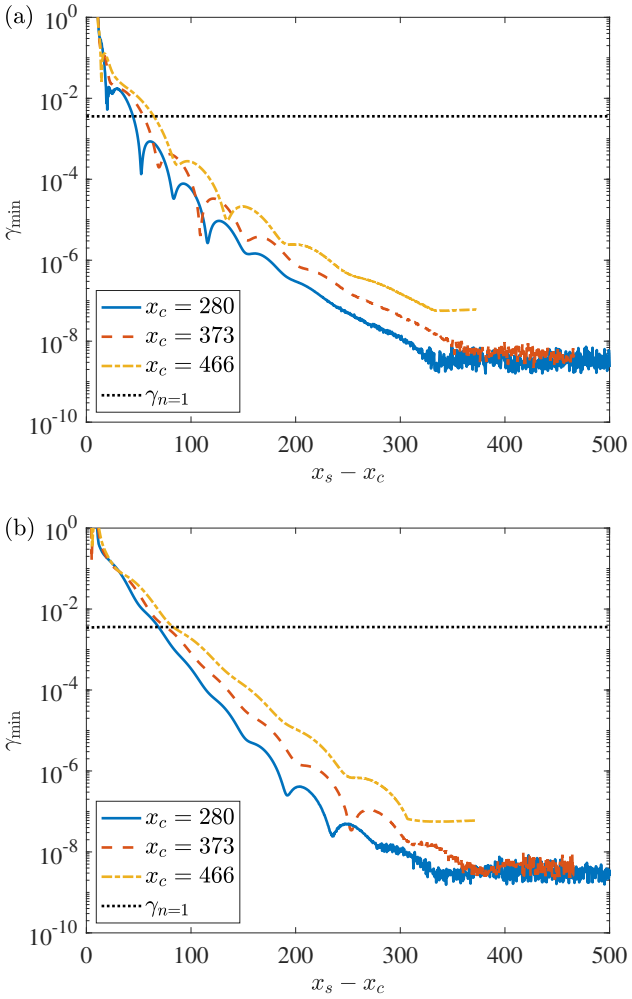


FIG. 9. Minimum value of the amplitude ratio, $\gamma_{\min}$, as a function of the sensor-control distance $x_s - x_c$, for a feedback system, where the sensor measurements are based on (a) the wall pressure p and (b) the wall shear stress $\partial u/\partial y$. Roughness and control settings match those conditions modelled in Fig. 4.

Computations were not significantly affected by the perturbation field measured by the sensor, particularly for sensor-control distances $x_s - x_c > 300$, where the amplitude ratio $\gamma_{\min}$ is of the order 10^{-8} in all cases modelled. Similar to Fig. 7, $\gamma_{\min}$ is characterised by numerical fluctuations for $x_s - x_c > 300$ that can again be attributed to round-off errors in the numerical solution that prevent further control benefits. Additionally, over the chord interval $x_s - x_c \in [0, 300]$, $\gamma_{\min}$

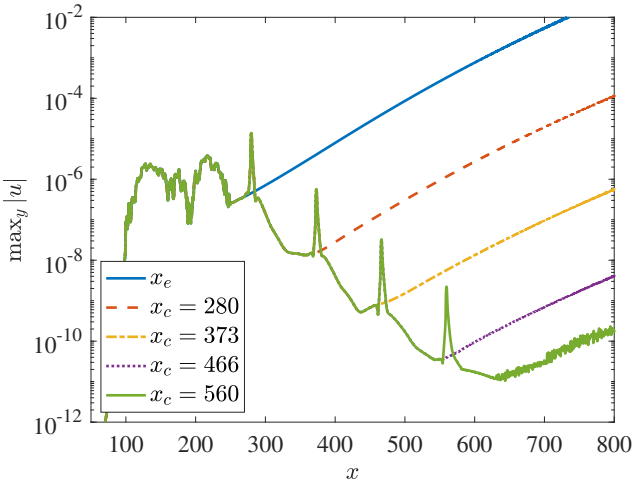


FIG. 10. Maximum absolute value of the u-velocity perturbation field for a stationary cross-flow instability established for the parameter settings $\{\bar{R}e, \beta\} = \{500, 0.4\}$. Perturbation excited by the surface roughness given in Fig. 3, with four control devices centred about $x_c = 280$, $x_c = 373$, $x_c = 466$, and $x_c = 560$, and four sensors fixed at $x_s = 326$, $x_s = 420$, $x_s = 513$, and $x_s = 606$, respectively.

decreases at an exponential rate.

Finally, the degree of amplitude damping obtained after one iteration is marginally less than those $\gamma_{\min}$ values realised in the chord region immediately downstream of the control mechanism; $x_s - x_c \lessapprox 70$. Thus, the feedforward method is the preferred modelling approach when the sensor is located very near the control device.

B. Multiple controllers

The above analysis suggests that LFC is improved if the control mechanism and sensor are located near the roughness strip and chord region that the cross-flow instability first emerges; the disturbance generated by the roughness strip has a reduced chord range to grow before the control device brings about amplitude damping. This might then allow for an array of control mechanisms and sensors implemented along the chord direction that bring about further amplitude reductions and control benefits.

To demonstrate the control benefits realised by a multiple controller set-up, a system of four control devices and four sensors is modelled. As before, the stationary cross-flow instability (with $\bar{R}e = 500$ and $\beta = 0.4$) is excited by the surface roughness plotted in Fig. 3. Four control mechanisms, with the same constant chord length $\lambda = \pi$, are fixed about four successive chord locations downstream of the roughness strip: $x_c = 280$, $x_c = 373$, $x_c = 466$ and $x_c = 560$. Based on the analysis presented above in Figs. 7-9, a sensor located 40 chord units downstream of each control device will establish an amplitude reduction γ of the order 10^{-3}-10^{-2} after one iteration of the sensor-control procedure. Consequently, four sensors are fixed about $x_s = 326$, $x_s = 420$, $x_s = 513$ and $x_s = 606$, respectively. Each sensor is used to relay disturbance measurements (based on the pressure perturbation field p at the wall) upstream to the preceding control mechanism.

Figure 10 displays the maximum absolute value of the u-velocity perturbation field, $\max_y |u|$, established by the roughness without and with the application of the four optimised control devices. The solid blue curve depicts the case where the four control mechanisms are turned off, while the remaining four line types (red dashed, yellow chain, purple dotted and green solid) display the solution after the first, second, third and fourth controllers are turned on and configured to optimal settings, respectively. Each control device is optimised after one iteration n only. The application of the first control device (centred about $x_c = 280$) brings about a 10^2-10^3 reduction in the disturbance amplitude (as expected given the results presented above in Figs 4-9). In addition, the second and third controllers (centred about $x_c = 373$ and $x_c = 466$) each bring about further amplitude reductions of the order 10^2-10^3. Finally, the fourth control device establishes a further reduction in the disturbance amplitude, but as a consequence of the computational precision of the numerical scheme, the control benefit is limited to the order 10^1-10^2. Much like those solutions presented above in Figs. 7 and 9, round-off errors are now significant. Consequently a fifth control device is unlikely to establish any further control benefits. Thus, the amplitude ratio parameter γ is approximately 10^{-10}-10^{-9} after the application of all four control mechanisms. Hence, considerable LFC is again achieved.

Contour plots of the disturbance development, $u/\max_y |u|$, associated with the above roughness-sensor-control settings, are illustrated in Fig. 11. The stationary cross-flow instability established by only the surface roughness is plotted in Fig. 11(a), with the inclusion of the first, second, third and forth control mechanisms depicted in the remaining four subplots chronologically down the figure. Similar to those contour plots presented in Fig. 6, the disturbance splits into two components over the chord interval that each control device suppresses the growth of the disturbance, i.e. those regions between successive controllers. Downstream of the fourth control mechanism (that is, $x > 700$ in Fig. 11(e)), the two components recoalesce to form the cross-flow instability. However, as a consequence of round-off errors coupled to the significant level of amplitude damping, the disturbance is characterised by fluctuations.

C. Sensor error

A sensors ability to accurately measure the amplitude and phase of the disturbance development is critical to the success of the control mechanism achieving amplitude damping and suppressing the onset of laminar-turbulent transition. However, systematic errors in the sensor measurements are to some degree unavoidable and will influence the control mechanisms efficiency and performance. Systematic errors may be caused by the observational equipment, a flawed configuration or some other unforeseen mechanism that is possibly brought about by the local environment.

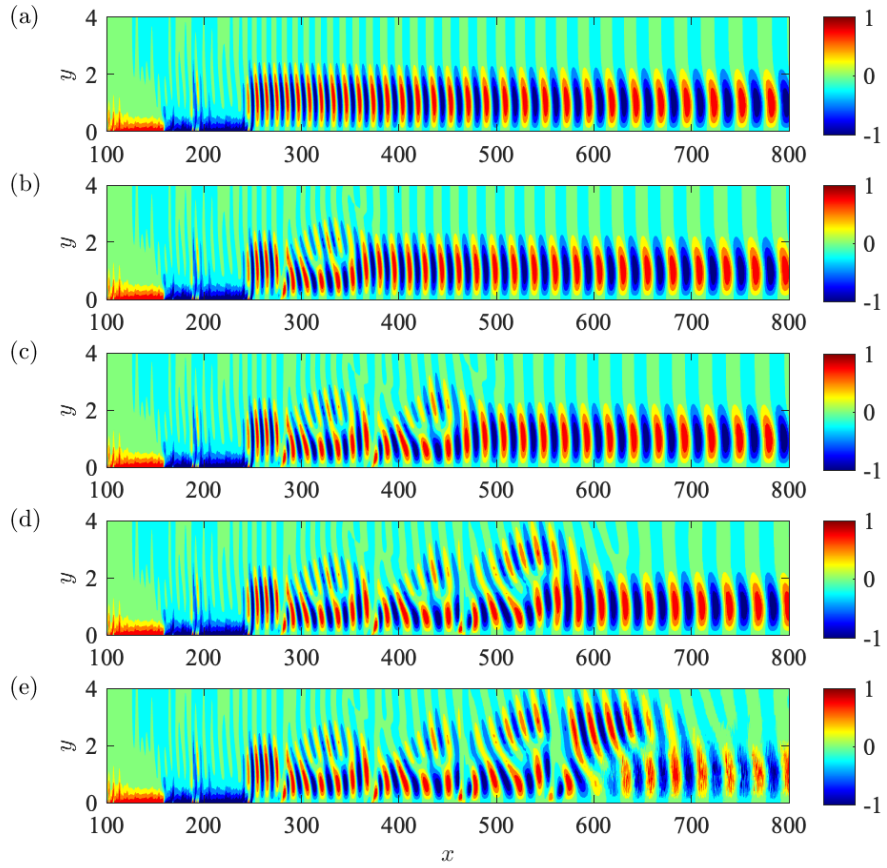


FIG. 11. Disturbance development $u/\max_y|u|$ in the (x,y)-plane, corresponding to the stationary cross-flow instability modelled in Fig. 10. Solution with each successive control device configured after one iteration. (a) No control device, and with control devices turned on and centred about (b) $x_c = 280$, (c) $x_c = 373$, (d) $x_c = 466$, and (e) $x_c = 560$.

The systematic error ε in a sensors measuring capability can (to name a few) be constant, random or proportional to the exact value of the disturbance field $\boldsymbol{q}_n$ (recall Eq. (8)). For simplicity we assume that the sensor error ε is given by the latter method. Thus, the disturbance measurement obtained by the sensor, with an internal error ε, is given as

$$\boldsymbol{q}_{n,\varepsilon} = (1+\varepsilon)\boldsymbol{q}_n. \tag{30}$$

To illustrate the effect of sensor error on the robustness of the control mechanism, we reconsider the one controller model presented in Fig. 4 for the stationary cross-flow instability

$$(\bar{Re},\beta) = (500, 0.4)$$

with control-sensor settings

$$(x_c, x_s) = (280, 480).$$

For this particular sensor-control set-up, it was shown that for a perfectly configured sensor (i.e., $\varepsilon = 0$), $\gamma_{\min} \sim O(10^{-7})$ was achieved after $n = 3$ iterations. The response to the inclusion of sensor error in this model is depicted in Fig. 12. Figure 12(a) displays the amplitude ratio γ obtained after three iterations n, as a function of the error ε. Solutions along the vertical axes are plotted on a logarithmic scale. Reasonable amplitude reductions, $\gamma \sim O(10^{-3})$ and less, are realised when the system error $\varepsilon < 0.1$. However, very little control benefits are realised for $\varepsilon > 0.5$, while for errors greater than unity the control mechanism has an unfavorable effect and increases the disturbance amplitude; $\gamma > 1$. This latter result is to be expected given how the sensor error is implemented in Eq. (30).

Figure 12(b) depicts the number of iterations n that are required to successfully achieve the greatest possible amplitude reduction; $\gamma_{\min} \sim O(10^{-7})$ for the above model settings. Clearly, for sensor errors $\varepsilon > 1$, the control mechanism enhances the disturbance amplitude, which will inevitably trigger the premature onset of laminar-turbulent transition. On the other hand, for $\varepsilon < 1$, significant levels of flow control are still realisable, but at a computational cost due to an increase in the number of iterations n in the sensor-control iterative

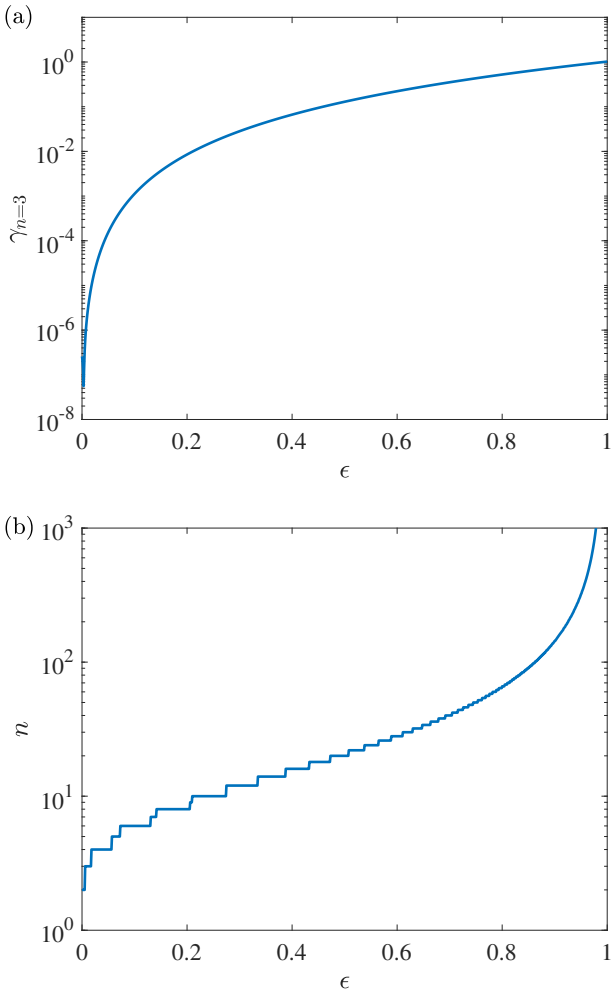


FIG. 12. (a) Amplitude ratio γ after three iterations and (b) number of iterations n required to achieve $\gamma \sim O(10^{-7})$, as a function of the error ε. Solutions matched to the roughness-control-sensor arrangement modelled in Fig. 4.

procedure. Ten or fewer iterations are required to achieve the greatest level of flow control when $\varepsilon < 0.25$. However, for errors ε greater than 0.5 and 0.8 the computational expense rises rapidly and the number of required iterations n increases sharply, to more than 25 and 100, respectively.

VII. CONCLUSIONS

A numerical investigation has been undertaken on the active control of linear stationary cross-flow vortices excited by surface roughness. Using solutions of the forward and adjoint linearised Navier–Stokes equations, both feedforward and feedback loop systems were modelled using the exciter-sensor-control arrangement illustrated in Fig. 1. The control mechanism was located downstream of the sensor for the feedforward model, while the set-up was reversed for the feedback modelling approach.

Linear stationary cross-flow disturbances were first excited by surface roughness. A sensor, located downstream of the roughness, measures the local amplitude and phase of the perturbation field. Sensor measurements were based on either the wall pressure or the wall shear stress. Amplitude and phase measurements were then relayed to the control device and laminar flow control was achieved using a localised wall modulation. However, similar levels of control would be achieved using other laminar flow control technologies; i.e. local suction holes or strips, plasma actuation or wall temperature panels. On coupling the sensor measurements with the solutions of the adjoint linearised Navier–Stokes equations, the control mechanism was switched on with the amplitude and phase shift necessary to establish destructive wave interference. For the feedforward modelling approach, control settings were configured at the first attempt. However, for the feedback loop system, the sensor remeasures the disturbance field and the local wall motion was reconfigured to further optimise laminar flow control. This process was repeated until no further control advantages were realised.

A significant level of flow control was achieved for both the feedforward and feedback loop systems, providing the sensor-control distances were sufficiently large. Reduced levels of flow control were obtained when the sensor was located immediately downstream of the control device. Additionally, results suggest that fixing the control device and sensor nearer the roughness strip and the region that the cross-flow instability first emerges, will establish greater control benefits.

For a perfectly configured sensor the amplitude of the stationary cross-flow instability was reduced by two to three orders of magnitude per iteration. Amplitude reductions of the order 10^3 were realisable for the feedforward method, while the amplitude of the cross-flow vortex was reduced by several orders of magnitude within only a few iterations of the feedback iterative procedure. Comparable levels of flow control were also realised for a multiple controller configuration.

For a single controller set-up, the degree of laminar flow control realised in this study was bounded and unchanged by applying further iterations or by increasing the sensor-control distance beyond that illustrated in Figs. 7-9. The same was true for a multiple controller arrangement. Thus, destructive wave interference was never fully realised. However, it was concluded by Thomas[16] that the interaction of the primary wave with other background disturbances prevented the absolute control of TS waves in his wind-tunnel experiments over a flat plate. Hence, we might expect similar flow features to appear in the swept Hiemenz boundary layer that prevent the total control of the stationary cross-flow instability. Additionally, computational precision and numerical round-off errors may have reduced the flow control capabilities. (It is worth emphasising that the results presented herein were not affected by further increases in the computational specifications.) Nevertheless, amplitude reductions of the order 10^8 were still realisable. Thus, significant delays in the onset of laminar-turbulent transition may be achieved.

Although the above study was limited to the control of linear stationary cross-flow disturbances in the incompressible swept Hiemenz boundary layer, the strategy could easily be

extended to encompass other forms of disturbance (TS waves, travelling cross-flow), complex compressible flow systems[45] and aerofoil bodies[73,74]. Additionally, nonlinear effects were ignored that become significant as perturbations achieve larger magnitudes, which may impede the optimised control mechanisms ability to dampen disturbance development. (This provides another reason for why the control device and sensor should be located in the chord region that the stationary cross-flow instability first appears.) Thus, further analysis is required to test the implementation and viability of the control strategy with the inclusion of nonlinearity[75,76].

DATA AVAILABILITY STATEMENT

The data that support the findings of this study are available from the corresponding author upon reasonable request.

[1] M. Gad-el Hak, "Modern developments in flow control," Appl. Mech. Rev. **49**, 365–379 (1996).

[2] R. D. Joslin, "Aircraft laminar flow control," Ann. Rev. Fluid Mech. **30**, 1–29 (1998).

[3] D. Arnal and J. P. Archambaud, "Laminar-turbulent transition control: NLF, LFC, HLFC." in *In Advances in Laminar-Turbulent Transition Modeling. VKI Lecture Series* (Brussels, Belgium: Von Karman Institute for Fluid Dynamics, 2008).

[4] W. Saric, H. Reed, and E. J. Kerschen, "Boundary layer receptivity to freestream disturbances," Annu. Rev. Fluid Mech. **34**, 291–319 (2002).

[5] M. V. Morkovin, "On the many faces of transition," in *Viscous Drag Reduction: Proceedings of the Symposium on Viscous Drag Reduction held at the LTV Research Center, Dallas, Texas, September 24 and 25, 1968*, edited by C. S. Wells (Springer US, Boston, MA, 1969) pp. 1–31.

[6] T. Herbert, "Secondary instability of boundary layers," Annu. Rev. Fluid Mech. **20**, 487–526 (1988).

[7] W. Saric, H. Reed, and E. White, "Stability and transition of three-dimensional boundary layers," Annu. Rev. Fluid Mech. **35**, 413–440 (2003).

[8] L. N. Trefethen, A. E. Trefethen, S. C. Reddy, and T. A. Driscoll, "Hydrodynamic stability without eigenvalues," Science **261**, 578–584 (1993).

[9] P. J. Schmid, "Nonmodal stability theory," Annu. Rev. Fluid Mech. **39**, 129–162 (2007).

[10] D. Biau and A. Bottaro, "An optimal path to transition in a duct," Phil. Trans. R. Soc. A. **367**, 529–544 (2009).

[11] A. Sengupta, P. Sundaram, and T. K. Sengupta, "Nonmodal nonlinear route of transition to two-dimensional turbulence," Phys. Rev. Res. **2**, 012033 (2020).

[12] P. Sundaram, V. K. Suman, and T. K. Sengupta, A. Sengupta, "Effects of free stream excitation on the boundary layer over a semi-infinite flat plate," Phys. Fluids **32**, 094110 (2020).

[13] R. R. Kerswell, "Nonlinear nonmodal stability theory," Annu. Rev. Fluid Mech. **50**, 319–345 (2018).

[14] H. W. Liepmann, G. L. Brown, and D. M. Nosenchuck, "Control of laminar-instability waves using a new technique," J. Fluid Mech. **118**, 187–200 (1982).

[15] H. W. Liepmann and D. M. Nosenchuck, "Active control of laminar-turbulent transition," J. Fluid Mech. **118**, 201–204 (1982).

[16] A. S. Thomas, "The control of boundary-layer transition using a wave-superposition principle," J. Fluid Mech. **137**, 233–250 (1983).

[17] E. Laurien and L. Kleiser, "Numerical simulation of boundary layer transition and transition control," J. Fluid Mech. **199**, 403–440 (1989).

[18] L. D. Kral and H. F. Fasel, "Numerical investigation of three-dimensional active control of boundary-layer transition," AIAA J. **29**, 1407–1417 (1991).

[19] L. Kleiser and E. Laurien, "Numerical investigation of interactive transition control," AIAA Paper 85–0566 (1985).

[20] R. D. Joslin, G. Erlebacher, and M. Y. Hussaini, "Active control of instabilities in laminar boundary layers – overview and concept validation," ASME J. Fluids Engng **118**, 494–497 (1996).

[21] M. Gad-el Hak, "Flow control: Passive, active and reactive flow management," (Cambridge, UK: Cambridge Univ.ersity Press, 2000).

[22] T. R. Bewley, "Flow control: new challenges for a new renaissance," Prog. Aerosp. Sci. **37**, 21–58 (2001).

[23] S. S. Collis, R. D. Joslin, A. Seifert, and V. Theofilis, "Issues in active flow control: theory, control simulation and experiment," Prog. Aerosp. Sci. **40**, 237–289 (2004).

[24] J. Kim and T. R. Bewley, "A linear systems approach to flow control," Ann. Rev. Fluid Mech. **39**, 383–417 (2007).

[25] S. Bagheri and D. S. Henningson, "Transition delay using control theory," Philos. Trans. Royal Soc. A **369**, 1365–1381 (2011).

[26] Y. Li and M. Gaster, "Active control of boundary-layer instabilities," J. Fluid Mech. **550**, 185–205 (2006).

[27] B. A. Belson, O. Semeraro, C. W. Rowley, and D. S. Henningson, "Feedback control of instabilities in the two-dimensional blasius boundary layer: The role of sensors and actuators," Phys. Fluids **25**, 054106 (2013).

[28] S. S. Joshi, J. L. Speyer, and J. Kim, "A systems theory approach to the feedback stabilization of infinitesimal and finite-amplitude disturbances in plane poiseuille flow," J. Fluid Mech. **332**, 157–184 (1997).

[29] T. R. Bewley and S. Liu, "Optimal and robust control and estimation of linear paths to transition," J. Fluid Mech. **365**, 305–349 (1998).

[30] H. Högberg, T. R. Bewley, and D. S. Henningson, "Linear feedback control and estimation of transition in plane channel flow," J. Fluid Mech. **481**, 149–175 (2003).

[31] R. D. Joslin, M. D. Gunzberger, and R. A. Nicolaides, "Self-contained automated methodology for optimal flow control," AIAA J. **35**, 816– (1997).

[32] H. Högberg and D. S. Henningson, "Linear optimal control applied to instabilities in spatially developing boundary layers," J. Fluid Mech. **470**, 151–179 (2002).

[33] G. A., P. J. Schmid, and P. Huerre, "Optimal energy growth and optimal control in swept hiemenz flow," J. Fluid Mech. **566**, 11–45 (2006).

[34] T. Herbert, "Parabolized stability equations," Annu. Rev. Fluid Mech. **29**, 245–283 (1997).

[35] P. Balakumar and P. Hall, "Optimum suction distribution for transition control," Theoret. Comput. Fluid Dyn. **13**, 1–19 (1999).

[36] S. Walther, C. Airiau, and A. Bottaro, "Optimal control of Tollmien–Schlichtlng waves in a developing boundary layer," Phys. Fluids **13**, 2087–2096 (2001).

[37] J. O. Pralits, A. Hanifi, and D. S. Henningson, "Adjoint-based optimisation of steady suction for disturbance control in incompressible flows," J. Fluid Mech. **467**, 129–161 (2002).

[38] J. O. Pralits and A. Hanifi, "Optimization of steady suction for disturbance control on infinite swept wings," Phys. Fluids **15**, 2756–2772 (2003).

[39] C. Airiau, A. Bottaro, S. Walther, and D. Legendre, "A methodology for optimal laminar flow control: Application o the damping of Tollmien–Schlichting waves in a boundary layer," Phys. Fluids **15**, 1131–1145 (2003).

[40] D. C. Hill, "Adjoint systems and their role in the receptivity problem for boundary layers," J. Fluid Mech. **292**, 183–204 (1995).

[41] A. Dobrinsky and S. S. Collis, "Adjoint parabolized stability equations for receptivity prediction," AIAA Paper , 2000–2651 (2000).

[42] P. Luchini and A. Bottaro, "Gortler vortices: a backward-in-time approach to the receptivity problem," J. Fluid Mech. **363**, 1–23 (1998).

[43] C. Airiau, "Non-parallel acoustic receptivity of a Blasius boundary layer using an adjoint approach," Flow, Turbulence and Combustion **65**, 347–367 (2000).

[44] F. Giannetti and P. Luchini, "Leading-edge receptivity by adjoint methods," J. Fluid Mech. **547**, 21–53 (2006).

[45] C. Thomas, S. Mughal, and R. Ashworth, "On predicting receptivity to surface roughness in a compressible infinite swept wing boundary layer," Phys. Fluids **29**, 034102 (2017).

[46] G. S. Brennan, J. S. B. Gajjar1, and R. E. Hewitt, "Tollmien–Schlichting wave cancellation via localised heating elements in boundary layers," J. Fluid Mech. **909**, A16 (2021).

[47] G. S. Brennan, J. S. B. Gajjar1, and R. E. Hewitt, "Cancellation of Tollmien–Schlichting waves with surface heating," J. Eng. Math. **128**, 5 (2021).

[48] T. C. Corke, C. L. Enloe, and S. P. Wilkinson, "Dielectric barrier discharge plasma actuators for flow control," Annu. Rev. Fluid Mech. **42**, 505–529 (2010).

[49]N. Benard and E. Moreau, "Electrical and mechanical characteristics of surface ac dielectric barrier discharge plasma actuators applied to airflow control," Exp. Fluids **55**, 1846 (2014).
[50]R. Dadfar, A. Hanifi, and D. S. Henningson, "Control of instabilities in an unswept boundary layer," AIAA J. **56**, 1750–1759 (2018).
[51]P. W. Carpenter and A. D. Garrad, "The hydrodynamic stability of flow over kramer-type compliant surfaces. Part 1. Tollmien–Schlichting instabilities," J. Fluid Mech. **155**, 465–510 (1985).
[52]C. Davies and P. W. Carpenter, "Numerical simulation of the evolution of Tollmien–Schlichting waves over finite compliant panels," J. Fluid Mech. **335**, 361–392 (1997).
[53]M. Amitay, B. A. Tuna, and H. Dell'Orso, "Identification and mitigation of T–S waves using localized dynamic surface modification," Phys. Fluids **28**, 064103 (2016).
[54]R. Erdmann, A. Pätzold, M. Engert, I. Peltzer, and W. Nitsche, "On active control of laminar turbulent transition on two-dimensional wings," Phil. Trans. R. Soc. A **369**, 1382–1395 (2011).
[55]M. I. Hussein, S. Biringen, O. R. Bilal, and A. Kucala, "Flow stabilization by subsurface phonons," Proc. R. Soc. A **471**, 20140928 (2015).
[56]S. K. Roberts and M. I. Yaras, "Boundary-layer transition affected by surface roughness and free-stream turbulence," J. Fluids Eng. **127**, 449–457 (2005).
[57]J. P. Bons, "A review of surface roughness effects in gas turbines," J. Turbomach. **132**, 021004 (2010).
[58]F. Montomoli, H. Hodson, and F. Haselbach, "Effect of roughness and unsteadiness on the performance of a new LPT blade at low Reynolds numbers," J. Turbomach. **132**, 031018 (2010).
[59]N. R. Vadlamani, R. Jefferson-Loveday, and P. G. Tucker, "Large eddy simulations in turbines: Influence of roughness and free-stream turbulence flow," Flow Turbulence Combust. **92**, 543–561 (2014).
[60]A. Sengupta, N. R. Vadlamani, and P. G. Tucker, "Roughness induced transition in low pressure turbines," (American Institute of Aeronautics and Astronautics Inc., 2017).
[61]M. S. Mughal, "Active control of wave instabilities in three-dimensional compressible flows," Theoret. Comput. Fluid Dyn. **12**, 195–217 (1998).
[62]S. M. Mughal and R. Ashworth, "Uncertainty quantification based receptivity modelling of crossflow instabilities induced by distributed surface roughness in swept wing boundary layers," (2013), AIAA Paper 2013-3106, 43rd AIAA Fluid Dynamics Conference, 2013. doi: 10.2514/6.2013-3106.
[63]C. Thomas and C. Davies, "An adjoint approach for computing the receptivity of the rotating disc boundary layer to surface roughness," J. Fluid Mech. **926**, A16 (2021).
[64]D. Van Deusen, "A statistical technique for the dynamic analysis of vehicles traversing rough yielding and non-yielding surfaces," NASA Rep. No. CR-659, 178 pages (1967).
[65]S. Sayles and T. R. Thomas, "Surface topography as a nonstationary random process," Nature **271**, 431–434 (1978).
[66]Y. Gong, S. T. Misture, P. Gao, and N. P. Mellott, "Surface roughness measurements using power spectrum density analysis with enhanced spatial correlation length," J. Phys. Chem. C **120**, 22358–22364s (2016).
[67]T. D. B. Jacobs, T. Junge, and L. Pastewka, "Quantitative characterization of surface topography using spectral analysis," Surface Topography: Metrology and Properties **5**, 013001 (2017).
[68]H. Raposo, S. Mughal, and R. Ashworth, "Acoustic receptivity and transition modeling of Tollmien–Schlichting disturbances induced by distributed surface roughness," Phys. Fluids **30**, 044105 (2018).
[69]R. H. J. Radeztsky, M. S. Reibert, and W. S. Saric, "Development of stationary crossflow vortices on a swept wing," AIAA Pap. Bo. 94–2373 (1999).
[70]S. Mughal, "Advanced transition prediction and development of linearised Navier–Stokes receptivity methods, validation and application," Tech. Rep. (Institute for Mathematical Sciences, Imperial College London, 2012) EADS-IW ref: IW102175.
[71]M. R. Malik, F. Li, and C. L. Chang, "Crossflow disturbances in three-dimensional boundary layers : nonlinear development, wave interaction and secondary instability," J. Fluid Mech. **268**, 1–36 (1994).
[72]C. Thomas, P. Hall, and C. Davies, "Nonlinear effects on the receptivity of crossflow in the swept hiemenz flow," J. Fluid Mech. **763**, 433–459 (2015).
[73]C. Thomas, S. Mughal, M. Gipon, R. Ashworth, and A. Martinez-Cava, "Stability of an infinite swept wing boundary layer with surface waviness," AIAA J. **54**, 3024–3038 (2016).
[74]C. Thomas, S. Mughal, H. Roland, R. Ashworth, and A. Martinez-Cava, "Effect of small surface deformations on the stability of tollmien–schlichting disturbances," AIAA J. **56**, 2157–2165 (2018).
[75]C. T. Pringle and R. P. Kerswell, "Using nonlinear transient growth to construct the minimal seed for shear flow turbulence," Phys. Rev. Lett. **105**, 154502 (2010).
[76]P. Luchini and A. Bottaro, "Adjoint equations in stability analysis," Annu. Rev. Fluid Mech. **46**, 493517 (2014).